Atomistic modeling of anharmonic phonon-phonon scattering in nanowires

Mathieu Luisier
Integrated Systems Laboratory, ETH Zürich, Gloriastrasse 35, 8092 Zürich, Switzerland
(Received 20 July 2012; revised manuscript received 25 October 2012; published 10 December 2012)

Phonon transport is simulated in ultrascaled nanowires in the presence of anharmonic phonon-phonon scattering. A modified valence-force-field model containing four types of bond deformation is employed to describe the phonon band structure. The inclusion of five additional bond deformation potentials allows us to account for anharmonic effects. Phonon-phonon interactions are introduced through inelastic scattering self-energies solved in the self-consistent Born approximation in the nonequilibrium Green's function formalism. After calibrating the model with experimental data, the thermal current, resistance, and conductivity of ⟨100⟩-, ⟨110⟩-, and ⟨111⟩-oriented Si nanowires with different lengths and temperatures are investigated in the presence of anharmonic phonon-phonon scattering and compared to their ballistic limit. It is found that all the simulated thermal currents exhibit a peak at temperatures around 200 K if phonon scattering is turned on while they monotonically increase when this effect is neglected. Finally, phonon transport through Si-Ge-Si nanowires is considered.

DOI: 10.1103/PhysRevB.86.245407 PACS number(s): 63.22.Gh, 65.80.−g

I. INTRODUCTION

The recent replacement of conventional planar Si metal-oxide-semiconductor field-effect transistors (MOSFETs) by three-dimensional (3D) transistors with a multigate configuration[1] has confirmed the leading role that nanowire-like structures will play in the future of Moore's scaling law.[2] Ultrascaled nanowires are not only expected to become the active components of next generation integrated circuits[3–7] due to their excellent electrostatic properties, but could also work as energy harvesters through the Seebeck effect if their surface is properly engineered.[8,9]

The main difference between nanowire transistors and thermogenerators resides in the value of their thermal conductivity κ_{th} which measures how efficiently heat can propagate through a material. While it is crucial to have a high κ_{th} for transistors so that the heat dissipated during ON-OFF switches can be rapidly evacuated from their active region, thermogenerators rely on a low κ_{th} that allows for an efficient conversion of the available heat into energy. Measurement techniques have evolved to the point where they can provide a deep insight into the thermal conduction of nanowires,[10,11] which is essential for both electronic and thermoelectric applications. At the same time the theoretical understanding of the thermal properties of nanowires has kept improving due to the development of always more complex and more accurate models.[12–23] In many cases, a direct comparison of experimental data and simulation results is possible.

Due to time constraints, computer aided design tools usually combine the classical drift-diffusion, energy-balance, and electrothermal models[24] to simulate the thermal properties of a device. However, at the nanometer scale, such approaches are no more valid and must be replaced by models treating thermal transport at the phonon level. Nowadays, most theoretical investigations of nanoscale thermal transport are based either (i) on the linearized Boltzmann transport equation with Fermi's golden rule[15,16,20,21] (phonon quantum confinement neglected), (ii) on equilibrium molecular dynamics simulations[23] (computationally very intensive and statistical average over long time periods required), (iii) on first-principles (*ab initio*) methods[19] (limited to very small systems), or (iv) on coherent phonon nonequilibrium Green's function (NEGF) approaches[12,17,22] (no dissipative interactions).

The versatility and flexibility of NEGF[25,26] make it one of the most widely spread and appreciated formalisms to solve quantum transport problems. Although NEGF lends itself naturally to the description of various scattering mechanisms,[27] taking into account incoherent effects such as the anharmonic decay of high-energy phonons into two low-energy particles, as required in thermal transport simulations, still represents a challenge from a physical and computational point of view. There have been some successful implementations of anharmonic phonon-phonon scattering in the framework of NEGF, but they have been restricted to very small, one-dimensional, atomic chains or molecular junctions.[13,14,18]

In this paper, an atomistic phonon transport approach based on the NEGF formalism, a modified valence-force-field (VFF) model, including anharmonic phonon-phonon scattering in the self-consistent Born approximation, and capable of treating three-dimensional nanowires composed of several thousands atoms is therefore presented. Realistic harmonic and anharmonic potential energies are used to construct the dynamical matrix of the considered systems and to compute the anharmonic phonon-phonon interactions. Hence, the model can accurately reproduce the bulk phonon band structure and lattice thermal conductivity of a given material.

In spite of the computational complexity, ultrascaled nanowires with a diameter of 3 nm, different crystal orientations (⟨100⟩, ⟨110⟩, and ⟨111⟩), lengths (20, 40, and 60 nm), temperatures (from 50 to 1000 K), and made of more than 20 000 atoms can be simulated within a couple of hours. As applications, the thermal current flowing through such nanowires as well as the resulting thermal resistance and conductivity are calculated. As key findings, it is shown that anharmonic phonon-phonon scattering in Si nanowires reduces their thermal conductivity by a factor 3–5 as compared to bulk structures and forces the thermal current to decrease for temperatures larger than 200 K (backscattering effect) while ballistic simulations predict an increase. The situation is reversed in heterogeneous Si-Ge-Si nanowires where anharmonic phonon scattering can lead to an increase of the

thermal current by opening additional propagating channels for phonons.

The paper is organized as follows: The NEGF-based phonon transport approach, the anharmonic phonon-phonon scattering self-energies, and the calculation of thermal currents are introduced in Sec. II. Then, in Sec. III, different types of Si and Si-Ge-Si nanowires are simulated in the ballistic limit of phonon transport and in the presence of anharmonic phonon-phonon scattering. Finally, conclusions are drawn in Sec. IV and an outlook on future work is presented.

II. THEORY

A. Model derivation

The nonequilibrium Green's function formalism is used to solve phonon transport with anharmonic phonon-phonon scattering. No electronic contribution is taken into account here because the influence of phonon-electron scattering on the thermal conductivity of lightly doped nanowires is negligible as compared to other scattering mechanisms.[28] This situation changes at higher electron concentrations, for which phonon-electron scattering becomes as important as other interactions. To avoid any confusion, all the structures considered in this work are assumed not intentionally doped.

In steady state, in a three-dimensional structure, the equations for the retarded $D_{nm}^{R,ij}(\omega)$ and greater/lesser $D_{nm}^{\gtrless,ij}(\omega)$ phonon Green's functions have the following form:[13,14,17,18]

$$\sum_k \sum_l \left[M_n\omega^2\delta_{ik}\delta_{nl} - \Phi_{nl}^{ik} - \Pi_{np}^{R,ik}(\omega)\right] D_{lm}^{R,kj}(\omega) = \delta_{ij}\delta_{nm}, \tag{1}$$

$$D_{nm}^{\gtrless,ij}(\omega) = \sum_{k_1k_2}\sum_{l_1l_2} D_{nl_1}^{R,ik_1}(\omega)\,\Pi_{l_1l_2}^{\gtrless,k_1k_2}(\omega)\,D_{l_2m}^{A,k_2j}(\omega). \tag{2}$$

In Eqs. (1) and (2), the indices l, l_1, l_2, m, and n run over atom positions, i, j, k, k_1, and k_2 over oscillation directions (x, y, and z), M_n is the mass of the atom at position $\mathbf{R}_n$, ω the phonon frequency, and $\Pi_{nm}^{R,ij}(\omega)$ the retarded self-energy including both an open boundary component $\Pi_{nm}^{RB,ij}(\omega)$ calculated as in Ref. 29 and a scattering component $\Pi_{nm}^{RS,ij}(\omega)$ derived later in this paper. Similarly, $\Pi_{nm}^{\gtrless,ij}(\omega) = \Pi_{nm}^{\gtrless B,ij}(\omega) + \Pi_{nm}^{\gtrless S,ij}(\omega)$ is the sum of the greater/lesser open boundary and scattering self-energy. The Φ_{nm}^{ij}'s are entries of the dynamical matrix $\mathbf{\Phi}$ of size $3N_A$, where N_A is the number of atoms in the simulation domain and 3 the number of degrees of freedom per atom, i.e., the number of directions along which atoms can oscillate (x, y, and z). They are defined as

$$\Phi_{nm}^{ij} = \frac{d^2V^{\text{harm}}}{dR_n^i dR_m^j}, \tag{3}$$

the second derivative of the valence-force-field (VFF) harmonic potential energy V^{harm} with respect to the ith component of the atom position $\mathbf{R}_n$ and the jth component of the atom position $\mathbf{R}_m$. A well-parametrized VFF model accurately describes all the phonon branches of a given material and can be therefore considered as a full-band approach. To ensure an accurate reproduction of the phonon band structure of group IV semiconductors, the VFF potential energy V^{harm} must include at least four bond interactions, bond stretching, bond bending, bond cross stretching, and coplanar bond bending, requiring four material parameters, as depicted in the upper part of Fig. 1. More information about the construction of $\mathbf{\Phi}$ and the harmonic force constants can be found in Refs. 30 and 31.

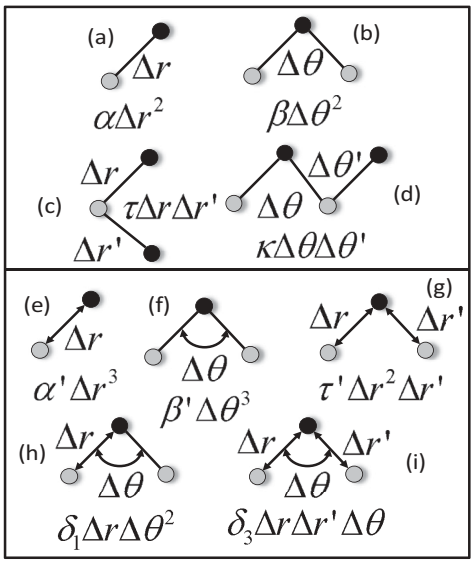

FIG. 1. Schematic representation of the different harmonic [(a)–(d)] and anharmonic [(e)–(i)] bond interactions included in the calculation of the phonon band structure and anharmonic phonon-phonon scattering self-energies, respectively. The term Δr describes bond length deformation, $\Delta\theta$ bond angle deformation. The material constants α, β, τ, κ, α', β', τ', δ_1, and δ_3 are empirical parameters whose values are determined by fitting available experimental targets.

The total Hamiltonian operator accounting for harmonic and anharmonic interactions can be written as[13]

$$\hat{H} = \frac{1}{2}\sum_i\sum_n M_n\hat{u}_n^i\hat{u}_n^i + \frac{1}{2}\sum_{ij}\sum_{mn}\Phi_{nm}^{ij}\hat{u}_n^i\hat{u}_m^j + \frac{1}{3!}\sum_{ijk}\sum_{lmn} dV_{lmn}^{(3)ijk}\hat{u}_l^i\hat{u}_m^j\hat{u}_n^k. \tag{4}$$

The first term on the right-hand side of Eq. (4) is the kinetic operator, the second one the harmonic operator, and the third one the anharmonic operator. The kinetic and harmonic operators directly appear in Eq. (1) while the anharmonic term is treated as a perturbation that can be cast into a scattering self-energy whose form still needs to be determined. The operator $\hat{u}_n^i$ represents the quantized displacement of an atom situated at $\mathbf{R}_n$ along the direction i (x, y, or z) measured with respect to its equilibrium position. The term $dV_{lmn}^{(3)ijk}$ contains the third derivative of the anharmonic potential energy V^{anh} as function of the ith component of the atom position $\mathbf{R}_l$, the jth component of the atom position $\mathbf{R}_m$, and the kth component of the atom position $\mathbf{R}_n$:

$$dV_{lmn}^{(3)ijk} = \frac{d^3V^{\text{anh}}}{dR_l^i dR_m^j dR_n^k}. \tag{5}$$

The anharmonic potential energy V^{anh} contains five bond interactions, as shown in the lower part of Fig. 1, leading to the following expression:[30]

$$V^{\text{anh}} = \frac{2}{3a_0^3}\sum_{mn}\alpha'\left(|\mathbf{R}_{mn}|^2 - \left|\mathbf{R}^0_{mn}\right|^2\right)^3 + \frac{2}{3a_0^3}\sum_{lmn}\beta'\left(\mathbf{R}_{lm}\cdot\mathbf{R}_{ln} - \mathbf{R}^0_{lm}\cdot\mathbf{R}^0_{ln}\right)^3 + \frac{2}{3a_0^3}\sum_{lmn}\tau'\left(|\mathbf{R}_{lm}|^2 - \left|\mathbf{R}^0_{lm}\right|^2\right)^2\left(|\mathbf{R}_{ln}|^2 - \left|\mathbf{R}^0_{ln}\right|^2\right)$$
$$+ \frac{2}{3a_0^3}\sum_{lmn}\delta_1\left(\mathbf{R}_{lm}\cdot\mathbf{R}_{ln} - \mathbf{R}^0_{lm}\cdot\mathbf{R}^0_{ln}\right)^2\left(|\mathbf{R}_{lm}|^2 - \left|\mathbf{R}^0_{lm}\right|^2\right) + \frac{2}{3a_0^3}\sum_{lmn}\delta_3\left(\mathbf{R}_{lm}\cdot\mathbf{R}_{ln} - \mathbf{R}^0_{lm}\cdot\mathbf{R}^0_{ln}\right)$$
$$\times\left(|\mathbf{R}_{lm}|^2 - \left|\mathbf{R}^0_{lm}\right|^2\right)\left(|\mathbf{R}_{ln}|^2 - \left|\mathbf{R}^0_{ln}\right|^2\right), \tag{6}$$

where $\mathbf{R}_{mn} = \mathbf{R}_n$-$\mathbf{R}_m$ is the bond vector connecting atoms m and n, $\mathbf{R}^0_{mn}$ the same bond vector when the atoms m and n are at their equilibrium position (no oscillation), a_0 the lattice constant of the material under consideration, and α', β', τ', δ_1, and δ_3 anharmonic force constants whose values are determined in Sec. III A. As demonstrated in Ref. 30, there exists more anharmonic interactions than those considered in Eq. (6), but they play a less important role than the five ones that are kept here.

To find an expression for the anharmonic phonon-phonon scattering self-energy in Eqs. (1) and (2), several steps need to be completed. The idea is to derive an equation of motion for the time-dependent phonon Green's function $D^{ij}_{nm}(t,t')$, which is proportional to the expectation value $\langle\hat{u}^i_m(t)\hat{u}^j_n(t')\rangle$, starting from the definition of the Hamiltonian operator $\hat{H}$ in Eq. (4). This leads to the formation of an infinite hierarchy of coupled equations: The expectation value of two operators depends on three operators whose expectation value depends on four operators and so forth. To truncate this infinite hierarchy, Wick's decomposition techniques and/or Feynman diagram expansions[32] can be applied. Finally, after Fourier-transforming the time difference $t - t'$, the steady-state form of the anharmonic phonon-phonon scattering self-energy is obtained. The greater/lesser components are then defined as[13,14]

$$\Pi^{\gtrless S,ij}_{nm}(\omega) = 2i\hbar\sum_{k_1k_2k_3k_4}\sum_{l_1l_2l_3l_4}\int_{-\infty}^{\infty}\frac{d\omega'}{2\pi}dV^{(3)ik_1k_2}_{nl_1l_2}dV^{(3)k_3k_4j}_{l_3l_4m}$$
$$\times D^{\gtrless,k_1k_3}_{l_1l_3}(\omega+\omega')D^{\lessgtr,k_4k_2}_{l_4l_2}(\omega'). \tag{7}$$

Knowing that "$\Pi^{<S}(\omega)D^{>}(\omega)$" measures the rate at which phonons with energy $\hbar\omega$ are generated (in-scattering rate)[33] and looking at the definition of $\Pi^{<S}(\omega)$ in Eq. (7), it can be seen that for $\omega' > 0$, the anharmonic decay of a high-energy phonon with frequency $\omega+\omega'$ $[D^{<}(\omega+\omega')]$ creates two lower energy phonons with frequency ω $[D^{>}(\omega)]$ and ω' $[D^{>}(\omega')]$. This interpretation relies on the fact that lesser Green's functions characterize the occupancy of a state while greater Green's functions refer to the probability that a state is available (unoccupied). Hence, at the beginning of the anharmonic phonon-phonon scattering process described above, the state with frequency $\omega+\omega'$ is occupied while two states at frequencies ω and ω' are available. Recalling that $D^{<,ij}_{nm}(-\omega) = D^{>,ji}_{mn}(\omega)$,[34] the same kind of interpretation can be made for the case where $\omega' < 0$, the difference being that a high-energy phonon is created from two low-energy particles through anharmonic interactions. Hence, the scattering self-energies in Eq. (7) simultaneously describe the anharmonic decay and creation of high-energy phonons.

The last required component in Eqs. (1) and (2), the retarded scattering self-energy $\Pi^{RS}(\omega)$, is calculated directly from the lesser $\Pi^{<S}(\omega)$ and greater $\Pi^{>S}(\omega)$ self-energies with

$$\Pi^{RS,ij}_{nm}(\omega) = \frac{1}{2}\left[\Pi^{>S,ij}_{nm}(\omega) - \Pi^{<S,ij}_{nm}(\omega)\right]$$
$$+ i\mathcal{P}\int\frac{d\omega'}{2\pi}\frac{\Pi^{>S,ij}_{nm}(\omega') - \Pi^{<S,ij}_{nm}(\omega')}{\omega-\omega'}, \tag{8}$$

where $\mathcal{P}$ denotes the Cauchy principal integral value.

Equations (1), (2), (7), and (8) must be solved iteratively till convergence between the Green's functions $D^{<}(\omega)$, $D^{>}(\omega)$, and $D^{R}(\omega)$ and the anharmonic phonon-phonon scattering self-energies $\Pi^{<S}(\omega)$, $\Pi^{>S}(\omega)$, and $\Pi^{RS}(\omega)$ is obtained. This process is called the self-consistent Born approximation. After convergence is reached, the phonon thermal current $I_{\text{ph},s->s+1}$ flowing between the sth and sth+1 unit cell (or slab) of the simulation domain can be computed as[17,37]

$$I_{\text{ph},s->s+1} = \frac{\hbar}{2\pi}\sum_{n\in s}\sum_{m\in s+1}\sum_{ij}$$
$$\times\int_0^{\infty}d\omega\,\omega\left[\Phi^{ij}_{nm}D^{<,ji}_{mn}(\omega) - D^{<,ij}_{nm}(\omega)\Phi^{ji}_{mn}\right]. \tag{9}$$

In Eq. (9), the atom position $\mathbf{R}_n$ is situated inside the sth unit cell and $\mathbf{R}_m$ inside the sth + 1 one. A unit cell is defined as an ensemble of N consecutive atomic layers along the direction of the current flow: $N = 4$ if phonon transport occurs along the $\langle 100\rangle$ crystal axis, $N = 2$ for $\langle 110\rangle$, and $N = 6$ for $\langle 111\rangle$. Due to current conservation requirements, $I_{\text{ph},s->s+1}$ must remain the same, irrespective of the choice of s and $s+1$.

B. Approximations

The expression for the anharmonic phonon-phonon scattering self-energy in Eq. (7) is exact, but difficult to implement from a numerical point of view. In effect, it involves the summation over several indices (4 referring to atom positions and 4 to oscillation directions), it requires the knowledge of the entire lesser and greater phonon Green's function matrices $\mathbf{D}^{<}(\omega)$ and $\mathbf{D}^{>}(\omega)$, respectively, and it couples all the phonon frequencies together through the integral over ω'. If no approximation is made to the calculation of the scattering

self-energies, the simulation of a nanowire structure composed of 20 000 atoms demands the inversion of full matrices of size $N = 60\,000$ to solve Eq. (1). The resulting computational burden is too heavy to make such an approach practical.

To allow for an efficient solution of Eqs. (1) and (2), only a small fraction of $\mathbf{D}^R(\omega)$ and $\mathbf{D}^{\gtrless}(\omega)$ is calculated, their diagonal and first off-diagonal blocks, based on a recursive Green's function (RGF) algorithm.[35,36] This implies that the scattering self-energies in Eq. (7) must be assumed block diagonal, i.e., only the self-energy components $\Pi^{\gtrless S,ij}_{nm}(\omega)$ where the atom indices n and m are identical are evaluated. As a consequence, the expression for $\Pi^{\gtrless S}(\omega)$ becomes

$$\Pi^{\gtrless S,ij}_{nn}(\omega) = 2i\hbar \sum_{k_1k_2k_3k_4} \sum_{lm} \int_{-\infty}^{\infty} \frac{d\omega'}{2\pi} dV^{(3)ik_1k_2}_{nlm} dV^{(3)k_3k_4j}_{lmn} \times D^{\gtrless,k_1k_3}_{ll}(\omega+\omega') D^{\lessgtr,k_4k_2}_{mm}(\omega'). \quad (10)$$

Note that in Eq. (10), only summations over the 3×3 diagonal blocks of the phonon Green's functions $\mathbf{D}^{\gtrless}(\omega)$ are performed. To further reduce the computational complexity and the memory requirement, the three indices l, m, and n of the third derivative of the anharmonic potential energy, $dV^{(3)}_{lmn}$, must refer to atoms belonging to the same bond vector. At least two out of the three indices are therefore identical. As a last approximation, the principal integral term in Eq. (8) is neglected.

The simplifications leading to Eq. (10) certainly affect the simulation results and might lead to an overestimation or underestimation of the phonon thermal current I_{ph} flowing through the simulated nanostructures. However, a correction mechanism can still be introduced: The anharmonic force constants α', β', τ', δ_1, and δ_3 in Eq. (6) can be fitted so that available experimental data, for example the bulk lattice thermal conductivity of a given semiconductor, are accurately reproduced by the model. By doing so, the errors resulting from the approximations made to Eq. (10) are partly compensated. The fitting process is explained in more detail in Sec. III A.

C. Implementation

If multiple central processing units (CPUs) are available, the solution of Eqs. (1), (2), (8), and (10) can be parallelized using the message passing interface (MPI)[38] standard and the same work distribution scheme as in Ref. 39: Depending on the size of the available machine, only a small number of phonon frequencies is attributed to each CPU, which stores the corresponding Green's functions and scattering self-energies. Then, to compute $\Pi^{\gtrless S}(\omega)$ in Eq. (10), data must be exchanged between the different CPUs storing $D^{\lessgtr}(\omega+\omega')$ and $D^{\gtrless}(\omega')$. The nanowire simulations reported in Sec. III were run on 3000 CPUs during 2 to 12 hours.

Typically, an energy vector starting at $E = \hbar\omega = 0$ eV and extending up to the maximum phonon energy of the considered material (plus a small offset) is generated at the beginning of each simulation. The distance between two energy points is constant and amounts to 0.1 meV at most. As can be seen in the integral boundaries of Eq. (10), the frequency ω' in $D^{\gtrless}(\omega')$ can be negative, but for convenience, the selected energy vector starts at $E = 0$. The negative frequencies/energies are properly handled by recalling the property $D^{<,ij}_{nm}(-\omega) = D^{>,ji}_{mn}(\omega)$ already mentioned above.

To check the convergence of the self-consistent Born iterations between the phonon Green's function in Eq. (2) and the anharmonic phonon-phonon scattering self-energies in Eq. (10), the values of the thermal current $I_{\text{ph},s->s+1}$ flowing between unit cell s and $s+1$ are analyzed. Convergence is reached when $I_{\text{ph},s->s+1}$ in Eq. (9) is the same for all the unit cells s, i.e., when current conservation is satisfied. Usually, between 10 and 100 iterations are required to reach this goal, depending on the structure temperature (low temperature means less scattering and therefore fewer iterations) and length (the shorter the fewer iterations).

III. RESULTS

A. Model calibration

To compensate for the approximations made to Eq. (10), the values of the five anharmonic force constants α', β', τ', δ_1, and δ_3 in Eq. (6) are tuned so that the bulk lattice thermal conductivity of the considered semiconductors can be reproduced by the simulation approach. Here, as an illustration, the Si parameters are optimized: Instead of adjusting each anharmonic force constant independently, the values of Ref. 30 are used as initial guesses and then scaled, all by the same factor F_{scal}. In this approach, only one single parameter needs to be determined, F_{scal}, not five, thus reducing the complexity of the fitting procedure.

To optimize the value of F_{scal}, the first challenge consists in simulating one-dimensional bulk structures instead of three-dimensional nanowires, as described so far in this paper. Solving Eqs. (1) and (2) for bulk is relatively straightforward: The dynamical matrix $\mathbf{\Phi}$ must account for the periodicity along the y and z axis (transport occurs along x), introducing a q_y and q_z dependence to the dynamical matrix, $\mathbf{\Phi} \rightarrow \mathbf{\Phi}(q_y,q_z)$, where the phonon wave vectors q_y and q_z span the entire first Brillouin zone (BZ). The thermal current I_{ph} in Eq. (9) is then obtained by summing up all the q_y and q_z contributions. To facilitate the summation, a square unit cell is chosen instead of the primitive one, making the BZ square too.

The difficulty to go from nanowire to bulk structures resides in the treatment of the lesser/greater scattering self-energies in Eq. (10). Anharmonic phonon-phonon scattering in bulk does not only couple all the phonon frequency together (integral over ω'), but also all the q_y and q_z wave vectors through a double summation over these parameters. Taking this double summation into account makes the numerical implementation of Eq. (10) for bulk cases much more difficult than for nanowires since many more phonon Green's functions are coupled to each other (frequency and momentum coupling). However, by increasing the size of the selected bulk unit cells along the y and z axes, the phonon band structure along q_y and q_z becomes folded,[40] thus automatically coupling different q_y and q_z wave vectors together.

Since the folding effect increases with the dimensions of the bulk unit cell, what remains to be determined is the minimum size of this unit cell that best mimics the q_y and q_z coupling induced by anharmonic phonon-phonon scattering. Practical tests have shown that increasing the size of the bulk unit

TABLE I. Temperature-independent value of the anharmonic force constants in Si and Ge.

	α' (eV/m^3)	β' (eV/m^3)	τ' (eV/m^3)	δ_1 (eV/m^3)	δ_3 (eV/m^3)
Si	−2.421e10	−1.082e10	−2.338e9	−2.323e9	6.656e9
Ge	−2.113e10	−5.323e9	−2.796e9	−1.735e8	1.225e9

cell beyond $(4L_y) \times (4L_z)$, where $L_y \times L_z$ is the size of the original square unit cell and 4 the multiplication factor along y and z, does not affect the results any more. Hence, wave vector coupling is captured in bulk simulations by working with unit cells 16× larger than the smallest one with a square shape. Then the q_y- and q_z-dependent Brillouin zone can be safely discretized using 6 points along each wave vector direction for a total of 36 grid points ranging from 0 to π/L_y and 0 to π/L_z.

As a next step, several simulations are performed to determine the value of F_{scal} so that the anharmonic phonon scattering model gives a room temperature lattice thermal conductivity of $\kappa_{\text{th}} \approx 150$ W/K/m for Si. The corresponding α', β', τ', δ_1, and δ_3 values are reported in Table I. However, assuming that these parameters are temperature independent does not allow us to capture the bulk κ_{th} of Si at temperatures T below 200 K and above 400 K. A good reproduction of $\kappa_{\text{th}}(T)$ from 20 to 1000 K is only possible if all the anharmonic force constants in Table I are multiplied by a temperature-dependent factor $f(T)$ defined as

$$f(T) = \begin{cases} \left(\frac{T}{300}\right)^{0.9}, & 0 \leqslant T \leqslant 200, \\ c_1 + c_2 T + c_3 T^2 + c_4 T^3, & 200 \leqslant T \leqslant 400, \\ 1 + 0.2\frac{T-300}{300}, & 400 \leqslant T \leqslant 1000, \end{cases} \tag{11}$$

and plotted in Fig. 2(a). The coefficients c_1 to c_4 are given in Table II. The form of $f(T)$ has been empirically derived: It has been first observed that the temperature behavior of the experimental $\kappa_{\text{th}}(T)$ for $T > 300$ K is different from $T < 300$ K. By comparing simulations results to experimental data, the forms $(T/300)^{0.9}$ and $1 + 0.2(T - 300)/300$ have been determined for $T \leqslant 300$ and $T \geqslant 300$, respectively. As a last enhancement, the behavior of $df(T)/dT$ in the region $200 \leqslant T \leqslant 400$ is smoothed to prevent discontinuities in the $\kappa_{\text{th}}(T)$ curves.

Making the anharmonic force constants α', β', τ', δ_1, and δ_3 temperature dependent is justified by the fact that the harmonic V^{harm} and anharmonic V^{anh} potential energies depend on the temperature, which has not been accounted for anywhere else in the model and by the fact that higher order anharmonic potential contributions have been neglected. Other phonon simulation approaches including anharmonic effects must also give a temperature dependence to their interaction potentials in order to reproduce experimental data.[16,41,42]

Finally, to capture the low-temperature maximum of the lattice thermal conductivity of bulk Si, boundary and impurity scattering must be introduced into the model. A single fitting potential value $V^{\text{bound/imp}} = 4.7$ meV/m^2 containing both effects is used for that purpose. Hence, the following boundary/impurity scattering self-energy must be added to Eq. (10):

$$\Pi_{nn}^{\gtrless \text{bound/imp},ij}(\omega) = |V^{\text{bound/imp}}|^2 D_{nn}^{\gtrless,ij}(\omega). \tag{12}$$

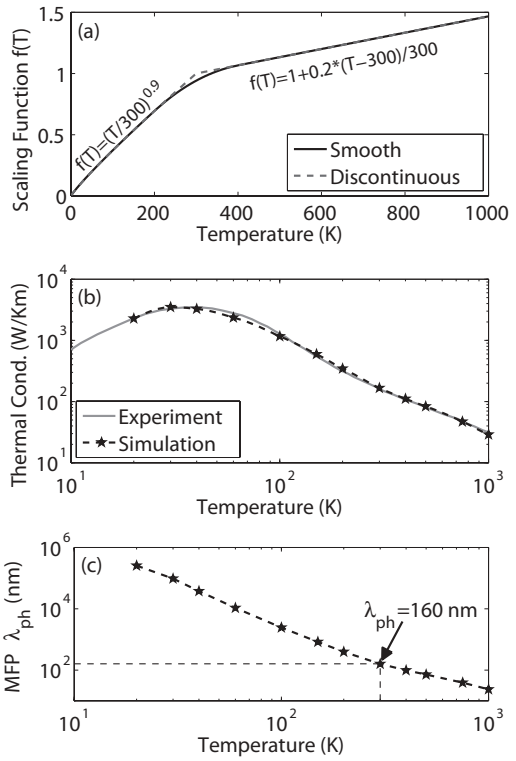

FIG. 2. (a) Temperature-dependent scaling function $f(T)$ for the anharmonic force constants α', β', τ', δ_1, and δ_3. (b) Comparison between the experimental lattice thermal conductivity κ_{th} of bulk Si as function of the temperature (solid line) and simulation results obtained with the model proposed in this paper (dashed line with stars). (c) Temperature-dependent average phonon mean-free path for scattering λ_{ph} in bulk Si extracted from the simulation results in (b). At 300 K, $\lambda_{\text{ph}} = 160$ nm.

Putting together all the requirements described above, κ_{th} of bulk Si can now be computed as a function of the temperature using the dR/dL method.[43] The following steps need to be performed one after the other to obtain κ_{th}:

(1) A small temperature difference ΔT is applied between the two ends of bulk structures of length $L = 25$, 50, and 75 nm.

(2) The length-dependent phonon thermal current $I_{\text{ph}}(L)$ (unit: W/m^2) flowing from one side of the structures to the other is calculated with Eq. (9) including anharmonic phonon-phonon, boundary, and impurity scattering.

(3) The thermal resistance $R_{\text{th}}(L) = \Delta T / I_{\text{ph}}(L)$ (unit: Km^2/W) is extracted. Since phonon transport in bulk structures is mainly diffusive, $R_{\text{th}}(L)$ increases linearly as a function of L. Three lengths are always considered to check that this property is satisfied.

(4) The derivative of $R_{\text{th}}(L)$ with respect to L, $dR_{\text{th}}(L)/dL$ (unit: Km/W), is finally employed to obtain the lattice thermal

TABLE II. Coefficients to compute the temperature-dependent factor $f(T)$ in Eq. (11).

	c_1	c_2	c_3	c_4
Value	−0.2097	5.98e−3	−7.644e−6	1.667e−9

conductivity $\kappa_{th} = [dR_{th}(L)/dL]^{-1}$ (unit: W/K/m). The same process is repeated for different temperatures.

The results for bulk Si are shown in Fig. 2(b). A very good agreement between experimental[44] and simulation data is obtained for temperatures ranging from 20 to 1000 K. Furthermore, an average mean-free path (MFP) for scattering λ_{ph} can be derived from the simulation results based on the following equation:[45]

$$\lambda_{ph} = \left(\frac{dR_{th}(L)}{dL}\right) \times R_{th,0}, \tag{13}$$

where the length-independent term $R_{th,0}$ refers to the ballistic thermal resistance extracted when all the scattering mechanisms are turned off. The average MFP λ_{ph} is plotted in Fig. 2(c) as function of the structure temperature. The results agree well with data calculated with another method.[46]

B. Homogeneous Si nanowires

After parametrizing the anharmonic force constant in Eq. (6) and assuming that these parameters are transferable to nanostructures, the thermal properties of not intentionally doped Si nanowires, as depicted in Fig. 3, are investigated in the ballistic limit of transport and in the presence of anharmonic phonon-phonon scattering. Boundary scattering is automatically taken into account due to the finite extent of the simulated structures which have a diameter of 3 nm. The nanowire length extends from 20 to 60 nm and phonon transport occurs along the x direction, aligned either with the ⟨100⟩, ⟨110⟩, or ⟨111⟩ crystal axis. The largest simulation domain considered in this work contains more than 20 000 atoms that can oscillate along the x, y, and z directions. Surface atoms are also allowed to freely move.[31]

Before starting with the thermal characteristics of the nanowires in Fig. 3, the mechanism governing the injection of phonons from semi-infinite contacts into a finite simulation domain should be analyzed. For that purpose, the thermal current and phonon population in a $L = 40$ nm long Si nanowire with $x = \langle 100 \rangle$ and a left (right) contact temperature of 300 K (350 K) are studied. The temperature difference between the left and right contact is intentionally chosen very high to magnify what is happening. There are three distinct cases:

(1) Phonon transport is ballistic in the semi-infinite contacts and in the finite simulation domain (ballistic).

(2) It is ballistic in the semi-infinite contacts, but anharmonic phonon-phonon scattering is taken into account in the finite simulation domain (coherent injection).

(3) Anharmonic phonon-phonon scattering is included in the semi-infinite contacts and in the finite simulation domain. This requires defining scattering self-energies in the contacts and incorporating them into the calculation of the open boundary conditions (incoherent injection).[47,48]

The differences between these three scenarios are illustrated in Fig. 4. In the pure ballistic simulation, the phonon population is the same all along the nanowire length, although the temperature of the left and right contact is different. When anharmonic phonon-phonon scattering is turned on, the phonon population becomes larger at the "hot" contact ($T = 350$ K) than at the cold one ($T = 300$ K), as expected. However, in the coherent injection case, due to domain mismatch at the contact/device interface, boundary reflections of the phonon population can be observed, which is unphysical and should be avoided. The distribution of the phonon population looks reasonable (smooth behavior) only when scattering is present in the nanowire structure and in the contacts. Hence, incoherent injection is enabled in all the other simulations performed in this paper.

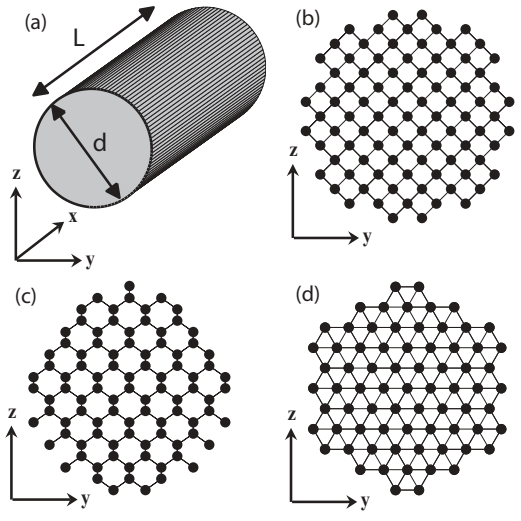

FIG. 3. (a) Schematic view of the Si nanowires considered in this work. The diameter d is set to 3 nm, the length L varies from 20 to 60 nm, the transport direction x is aligned with the ⟨100⟩ (b), ⟨110⟩ (c), and ⟨111⟩ (d) crystal axis. In (b), $y = (010)$, $z = (001)$, in (c), $y = (110)$, $z = (001)$, and in (d), $y = (110)$, $z = (112)$.

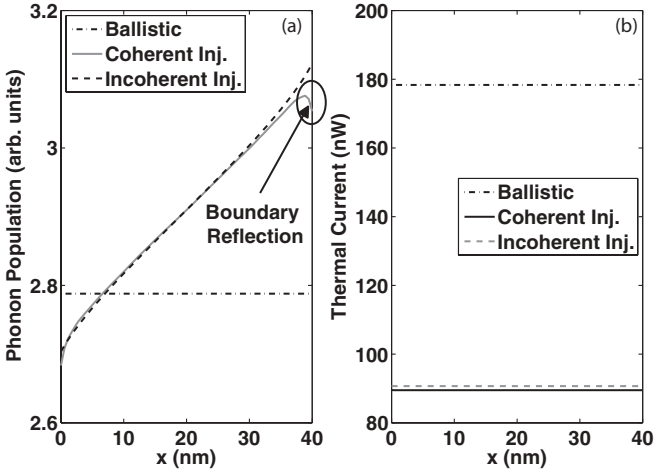

FIG. 4. (a) Spatially resolved phonon population in a $L = 40$ nm Si nanowire with $x = \langle 100 \rangle$, a left-contact ($x = 0$) temperature $T = 300$ K, and a right-contact ($x = 40$ nm) temperature $T = 350$ K. The phonon population in the ballistic limit of transport (dashed-dotted line), with anharmonic phonon-phonon scattering and ballistic contacts (coherent injection, solid gray lines), and with anharmonic phonon-phonon scattering in the device and contacts (incoherent injection, dashed line) are plotted. (b) Spatially resolved thermal current flowing through the same structure and under the same conditions as in (a).

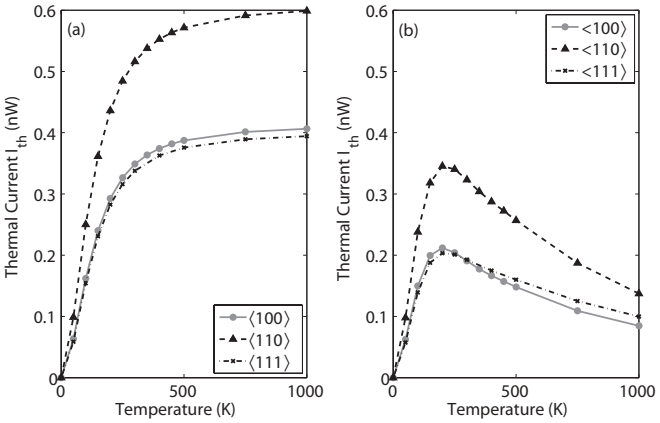

FIG. 5. (a) Temperature-dependent ballistic thermal current flowing through $L = 40$ nm Si nanowires with $x = \langle 100 \rangle$ (gray line with circles), $x = \langle 110 \rangle$ (dashed line with triangles), and $x = \langle 111 \rangle$ (dashed-dotted line with crosses). A temperature difference $\Delta T = 0.1$ K is applied between the 2 ends of the nanowires. (b) Same as in (a), but in the presence of anharmonic phonon-phonon scattering.

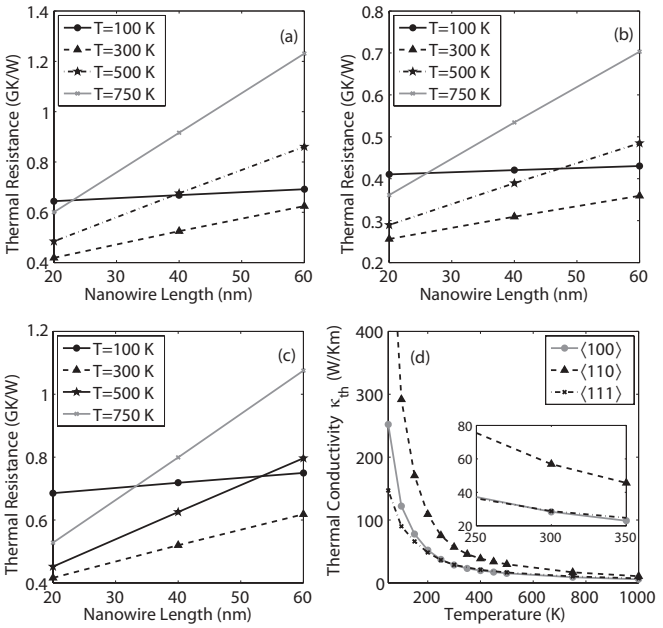

FIG. 6. (a) Thermal resistance through Si nanowires with $L = 20$, 40, and 60 nm, $T = 100$ (line with circles), 300 (dashed line with triangles), 500 (dashed-dotted line with stars), and 750 K (gray line with crosses), $\Delta T = 0.1$ K, $x = \langle 100 \rangle$, and in the presence of anharmonic phonon-phonon scattering. (b) Same as (a), but for $x = \langle 110 \rangle$. (c) Same as in (a) and (b), but for $x = \langle 111 \rangle$. (d) Anharmonic phonon-phonon limited thermal conductivity κ_{th} in Si nanowires as function of the temperature for $x = \langle 100 \rangle$ (gray line with circles), $x = \langle 110 \rangle$ (dashed line with triangles), and $x = \langle 111 \rangle$ (dashed-dotted line with crosses). The inset shows κ_{th} around $T = 300$ K.

A comment about the thermal currents in Fig. 4(b): In all cases, it is conserved, demonstrating the convergence of the self-consistent Born iterations between the phonon Green's functions and scattering self-energies in Eqs. (1), (2), (8), and (10). Current conservation has been checked for all the results presented here. Note also that anharmonic phonon-phonon scattering decreases the magnitude of the thermal current by a factor of roughly 2 in Fig. 4(b) and the coherent and incoherent phonon injection mechanisms deliver about the same current value.

In Fig. 5, the thermal current I_{ph} (unit: W) flowing through $L = 40$ nm long Si nanowires with transport along the $\langle 100 \rangle$, $\langle 110 \rangle$, and $\langle 111 \rangle$ crystal axes is reported for temperatures ranging from 0 to 1000 K, in the ballistic limit of transport (left) and with anharmonic phonon-phonon scattering (right). A temperature difference $\Delta T = 0.1$ K is applied between the two ends of the nanowires. Irrespective of the simulation model (without scattering), the $\langle 110 \rangle$-oriented nanowire exhibits the largest thermal current; the $\langle 100 \rangle$- and $\langle 111 \rangle$-oriented structures have similar characteristics.

While the ballistic thermal currents keep increasing as the temperature increases, anharmonic phonon-phonon scattering leads to a maximum of I_{ph} at temperatures around 200 K followed by a current decrease. A similar behavior is reported in Refs. 13 and 18 where the thermal conductance of 1D Si atomic chains is calculated: A conductance maximum occurs at temperatures around 200 K. The fact that scattering becomes more important at high temperatures explains the current decrease after $T = 200$ K. Hence, below 100 K, the ballistic model captures relatively well the thermal properties of the nanowires, but above this temperature, it significantly overestimates I_{ph}, by a factor of 1.7 at room temperature and 4 at 1000 K. It is worthwhile noting here that the thermal current shows a maximum at around $T = 200$ K even when the anharmonic force constants α', β', τ', δ_1, and δ_3 in Eq. (6) have no temperature dependence.

As for the bulk structures in Sec. III A, the thermal resistance $R_{th}(L)$ (unit: K/W) of the Si nanowires in Fig. 3 can be calculated for different structure lengths ($L = 20$, 40, and 60 nm) and temperatures varying from 50 to 1000 K. The corresponding results are shown in Figs. 6(a)–6(c). As a consequence of the larger thermal current observed when phonons flow along the $\langle 110 \rangle$ crystal axis, nanowires with this configuration have the smallest thermal resistances, at low and high temperatures.

Due to the diffusive nature of phonon transport in nanowires with anharmonic phonon-phonon scattering, their thermal resistance $R_{th}(L)$ increases linearly with their length: The resistance values at $L = 20$, 40, and 60 nm all lie on a single line as can be seen in Figs. 6(a)–6(c). This allows us to compute a phonon-phonon scattering limited lattice thermal conductivity $\kappa_{th} = (1/A)[dR_{th}(L)/dL]^{-1}$, where A is the area of the nanowire cross section. In Fig. 6(d), κ_{th} is given as function of the nanowire temperature and crystal orientation. The highest value is obtained for the $\langle 110 \rangle$-oriented nanowire. At low temperatures, the $\langle 100 \rangle$ nanowire exceeds its $\langle 111 \rangle$ counterpart, but this trend is reversed at high temperatures.

It can also be observed that under the influence of anharmonic phonon-phonon scattering, κ_{th} severely drops in nanowires as compared to bulk structures, from 148 W/K/m at room temperature down to 57, 29, and 28 W/K/m in $\langle 110 \rangle$, $\langle 111 \rangle$, and $\langle 100 \rangle$ nanowires, respectively. By comparing these simulation results with available experimental data, it appears that the phonon-phonon scattering limited thermal conductivities in Fig. 6(d) are considerably larger than the values reported in Ref. 8 (2 W/K/m at room temperature)

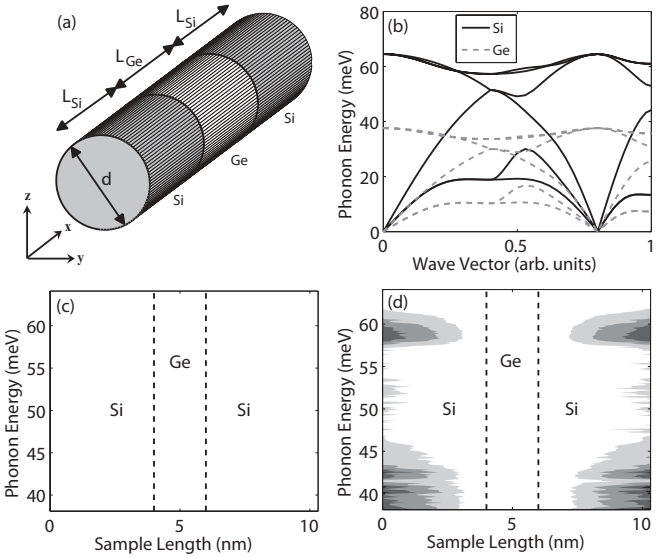

FIG. 7. (a) Schematic view of a Si-Ge-Si double heterojunction nanowire with $x = \langle 100 \rangle$ and $d = 3$ nm. The Ge region measures $L_{\mathrm{Ge}} = 2.2$ nm, the Si extensions vary from $L_{\mathrm{Si}} = 2.2$ to 10.9 nm. (b) Bulk Si (solid lines) and Ge (dashed lines) phonon band structure. (c) Ballistic spectral thermal current through a $L_{\mathrm{Si}} = 4.3$ nm Si-Ge-Si nanowire in the energy range $37 \leqslant E \leqslant 64$ meV at $T = 300$ K with $\Delta T = 10$ K. (d) Same as in (c), but in the presence of anharmonic phonon-phonon scattering. Dark regions indicate high current concentrations, white no current.

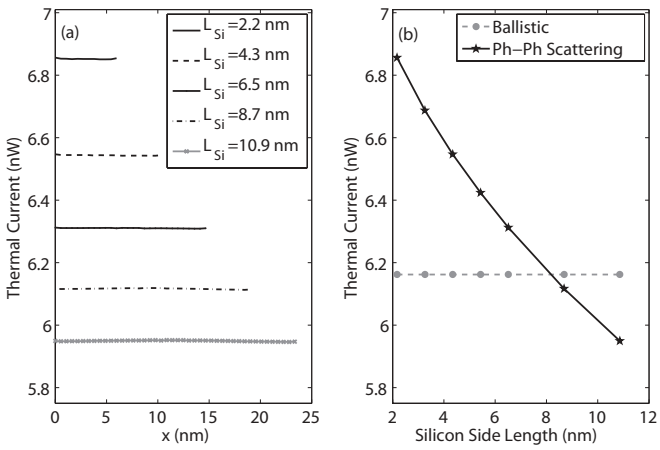

FIG. 8. (a) Spatially resolved thermal current through Si-Ge-Si nanowires with $T = 300$ K, $\Delta T = 10$ K, $L_{\mathrm{Si}} = 2.2$ (solid line), 4.3 (dashed line), 6.5 (solid line with dots), 8.7 (dashed-dotted line), and 10.9 nm (solid gray line with crosses) in the presence of anharmonic phonon-phonon scattering. (b) Thermal current flowing through Si-Ge-Si nanowires with $T = 300$ K, $\Delta T = 10$ K, and varying L_{Si}. The thermal currents in the ballistic limit of transport (dashed gray line with circles) and in the presence of anharmonic phonon-phonon scattering (solid line with stars) are compared.

although the considered diameters are much smaller (3 vs 50 nm). Hence, anharmonic phonon-phonon scattering alone cannot explain the results of Ref. 8, for which surface roughness must be added.[16]

C. Si-Ge-Si Nanowires

As a second application, the double heterojunction Si-Ge-Si nanowires schematized in Fig. 7(a) are considered. Such devices, if the Si-Ge periods are repeated as in superlattices, could exhibit very low thermal conductivities[20,49] while keeping relatively good electronic properties, thus fulfilling two important criteria needed for high-performance thermogenerators. Since the maximum phonon energy in Ge is smaller than in Si (37 vs 64 meV with the harmonic parameters of Ref. 30), as illustrated in Fig. 7(b), the high-energy phonons propagating through Si are blocked when they try to enter the Ge middle layer. This energy filtering effect leads to a reduction of the lattice thermal conductivity of Si-Ge-Si nanowires.

Here, what will be investigated is the influence of anharmonic phonon-phonon scattering on the thermal current flowing through Si-Ge-Si nanowires with a diameter of 3 nm, a Ge layer thickness of 2.2 nm, and Si extension lengths varying from $L_{\mathrm{Si}} = 2.2$ to 10.9 nm. The same scattering model is used for Ge as for Si with the anharmonic force constants of Ge given in Table I. They were obtained by scaling the values of Ref. 30 by the same amount as the Si constants. No temperature-dependent coefficient $f(T)$ has been defined for Ge since all the S-Ge-Si nanowire simulations are performed at room temperatures. Interface scattering is included by default since each material region is explicitly described in the simulation domain (different atomic masses, harmonic, and anharmonic force constants). Strain is also taken into account and no roughness is introduced at the Si/Ge interfaces, which are sharp.

In the ballistic model, a phonon with an energy larger than 37 meV cannot move through a Si-Ge-Si structure because of the absence of propagating channels in Ge in this energy range. When anharmonic phonon-phonon scattering is turned on, the same phonon can penetrate into the Si extensions, then decay into two low-energy particles that can finally propagate through the Ge layer. These two situations are plotted in Figs. 7(c)–7(d), where the energy- and position-resolved thermal current flowing through a Si-Ge-Si nanowire is reported for energies larger than 37 meV. As can be seen, the presence of anharmonic phonon-phonon scattering creates additional current trajectories at high energy that do not exist in the ballistic model.

As a last numerical experiment, the length of the Si extensions, L_{Si}, in Si-Ge-Si nanowires is varied to study how anharmonic phonon-phonon scattering influences the thermal current value. The results are shown in Fig. 8. In the left subplot, current conservation is demonstrated and in the right one, the thermal currents with and without anharmonic phonon-phonon scattering are compared. For short Si extensions, the thermal current with scattering is higher than the ballistic one, but it decreases as L_{Si} increases. The ballistic current remains constant. Two competing effects explain this behavior: Anharmonic phonon-phonon scattering opens additional transport channels for phonons, as depicted in Figs. 7(c)–7(d), but it can also change the direction of propagation of one of the two low particles created through the decay of a high-energy phonon, thus reducing the current magnitude. This is known as backscattering.[45] While the first effect (additional channels) does not depend on the Si length,

the second one (backscattering) increases with L_{Si}, explaining the current characteristics in Fig. 8(b).

IV. CONCLUSION AND OUTLOOK

A simulation approach including anharmonic phonon-phonon scattering in the framework of the valence-force-field method and the nonequilibrium Green's function formalism has been presented in this paper. After the calibration of anharmonic force constants using the temperature-dependent lattice thermal conductivity of Si as a target, the thermal properties of ultrascaled nanowires with different lengths, material composition, and crystal orientations have been studied. The thermal current, resistance, and conductivity of these structures have been extracted in the presence of anharmonic phonon-phonon scattering and in the ballistic limit of transport. It has been found that neglecting anharmonic phonon-phonon scattering at high temperatures can lead to a significant overestimation of the thermal current flowing through nanowires. Furthermore, it has also been demonstrated that in heterogeneous Si-Ge-Si nanowires, two competing effects induced by anharmonic phonon-phonon scattering face each other: an increase of the thermal current through the presence of additional phonon paths and a decrease of this current through backscattering effects. The first effect dominates in short devices, the second in long ones. This means that accurate studies about the figure of merit of thermogenerators or the thermal efficiency of nanotransistors should go beyond the ballistic limit of phonon transport and include anharmonic phonon-phonon interactions.

As a future work, the approach proposed here should be combined with an atomistic electron transport model taking electron-phonon scattering into account.[39] By simultaneously driving the electron and phonon populations out of equilibrium, self-heating and phonon drag effects could be introduced into the model. This will require the derivation of additional self-energies to control the energy flow between electrons and phonons and ensure energy conservation within the simulation domain.

ACKNOWLEDGMENTS

This work was supported by SNF Grant No. PP00P2_133591, by a grant from the Swiss National Supercomputing Centre (CSCS) under Project ID s363, by NSF Grant No. EEC-0228390 that funds the Network for Computational Nanotechnology, by NSF PetaApps Grant No. 0749140, and by NSF through XSEDE resources provided by the National Institute for Computational Sciences (NICS) and the Texas Advanced Computing Center (TACC). This research also used resources of the Oak Ridge Leadership Computing Facility at the Oak Ridge National Laboratory, which is supported by the Office of Science of the US Department of Energy under Contract No. DE-AC05-00OR22725.

[1] C. Auth *et al.*, in *IEEE Symposium on VLSI Technology* (IEEE, New York, 2012), p. 131.
[2] G. E. Moore, Electronics **38**, 114 (1965).
[3] Y. Cui, L. J. Lauhon, M. S. Gudiksen, J. Wang, and C. M. Lieber, Appl. Phys. Lett. **78**, 2214 (2001).
[4] A. B. Greytak, L. J. Lauhon, M. S. Gudiksen, and C. M. Lieber, Appl. Phys. Lett. **84**, 4176 (2004).
[5] S. D. Suk, S.-Y. Lee, S.-M. Kim, E.-J. Yoon, M.-S. Kim, M. Li, C. W. Oh, K. H. Yeo, S. H. Kim, D. S. Shin, K.-H. Lee, H. S. Park, J. N. Han, C. J. Park, J.-B. Park, D.-W. Kim, D. Park, and B.-I. Ryu, in *Electron Devices Meeting, 2005 (IEDM)* (IEEE, New York, 2005), p. 717.
[6] N. Singh, A. Agarwal, L. K. Bera, T. Y. Liow, R. Yang, S. C. Rustagi, C. H. Tung, and R. Kumar, IEEE Elec. Dev. Lett. **27**, 383 (2006).
[7] M. Li, K. H. Yeo, S. D. Suk, Y. Y. Yeoh, D.-W. Kim, T. Y. Chung, K. S. Oh, and W.-S. Lee, in *IEEE Symposium on VLSI Technology* (IEEE, New York, 2009), pp. 94-95.
[8] A. I. Hochbaum, R. Chen, R. Diaz Delgado, W. Liang, E. C. Garnett, M. Najarian, A. Majumdar, and P. Yang, Nature (London) **451**, 163 (2008).
[9] A. I. Boukai, Y. Bunimovich, J. Tahir-Kheli, J.-K. Yu, W. A. Goddard III, and J. R. Heath, Nature (London) **451**, 168 (2008).
[10] K. Hippalgaonkar, B. Huang, R. Chen, K. Sawyer, P. Ercius, and A. Majumdar, Nano Lett. **10**, 4341 (2010).
[11] L. Shi, Nanoscale Microscale Thermophysical Engineering **16**, 79 (2012).
[12] N. Mingo and L. Yang, Phys. Rev. B **68**, 245406 (2003).
[13] N. Mingo, Phys. Rev. B **74**, 125402 (2006).
[14] Y. Xu, J.-S. Wang, W. Duan, B.-L. Gu, and B. Li, Phys. Rev. B **78**, 224303 (2008).
[15] A. L. Moore, S. K. Saha, R. S. Prasher, and L. Shi, Appl. Phys. Lett. **93**, 083112 (2008).
[16] P. Martin, Z. Aksamija, E. Pop, and U. Ravaioli, Phys. Rev. Lett. **102**, 125503 (2009).
[17] T. Markussen, A.-P. Jauho, and M. Brandbyge, Phys. Rev. B **79**, 035415 (2009).
[18] J. Li, T. C. Au Yeung, C. H. Kam, Y. Peng, Q.-H. Chen, X. Zhao, and C. Q. Sun, J. Appl. Phys. **106**, 014308 (2009).
[19] A. Ward, D. A. Broido, D. A. Stewart, and G. Deinzer, Phys. Rev. B **80**, 125203 (2009).
[20] S. P. Hepplestone and G. P. Srivastava, Phys. Rev. B **82**, 144303 (2010).
[21] Z. Aksamija and I. Knezevic, Phys. Rev. B **82**, 045319 (2010).
[22] M. Luisier, J. Appl. Phys. **110**, 074510 (2011).
[23] Y. He and G. Galli, Phys. Rev. Lett. **108**, 215901 (2012).
[24] K. Souissi, F. Odeh, H. H. K. Tang, and A. Gnudi, COMPEL **13**, 439 (1994).
[25] L. P. Kadanoff and G. Baym, *Quantum Statistical Mechanics* (W. A. Benjamin, Inc., New York, 1962).
[26] L. V. Keldysh, Sov. Phys. JETP **20**, 1018 (1965).
[27] S. Datta, J. Phys.: Condens. Matter **2**, 8023 (1990).
[28] J. Zoua and A. Balandin, J. Appl. Phys. **89**, 2932 (2001).
[29] M. Luisier, A. Schenk, W. Fichtner, and G. Klimeck, Phys. Rev. B **74**, 205323 (2006).
[30] Z. Sui and I. P. Herman, Phys. Rev. B **48**, 17938 (1993).
[31] A. Paul, M. Luisier, and G. Klimeck, J. Comp. Elec. **9**, 160 (2010).
[32] A. Fetter and J. Walecka, *Quantum Theory of Many-Particle Systems* (McGraw-Hill Book Company, New York, 1971).

[33]S. Datta, *Electronic Transport in Mesoscopic Systems* (Cambridge University Press, Cambridge, UK, 1995).
[34]G. D. Mahan, *Many-Particle Physics* (Plenum, New York, 1990).
[35]R. Lake, G. Klimeck, R. C. Bowen, and D. Jovanovic, J. Appl. Phys. **81**, 7845 (1997).
[36]A. Svizhenko, M. P. Anantram, T. R. Govindan, B. Biegel, and R. Venugopal, J. Appl. Phys. **91**, 2343 (2002).
[37]M. Luisier and A. Schenk, J. Comput. Theor. Nanosci. **5**, 1031 (2008).
[38]W. Gropp, E. Lusk, N. Doss, and A. Skjellum, Parallel Computing **22**, 789 (1996).
[39]M. Luisier and G. Klimeck, Phys. Rev. B **80**, 155430 (2009).
[40]T. B. Boykin and G. Klimeck, Phys. Rev. B **71**, 115215 (2005).
[41]M. Holland, Phys. Rev. **132**, 2461 (1963).
[42]N. Mingo, Phys. Rev. B **68**, 113308 (2003).
[43]K. Rim, S. Narasimha, M. Longstreet, A. Mocuta, and J. Cai, in *Electron Devices Meeting, 2002 (IEDM)* (IEEE, New York, 2002), pp. 43–46.
[44]C. J. Glassbrenner and G. A. Slack, Phys. Rev. A **134**, 1058 (1964).
[45]M. S. Lundstrom, IEEE Elec. Dev. Lett. **22**, 293 (2001).
[46]C. Jeong, S. Datta, and M. Lundstrom, J. Appl. Phys. **109**, 073718 (2011).
[47]M. Frey, A. Esposito, and A. Schenk, *Proceedings of the 13th International Workshop on Computational Electronics (IWCE-13)* (IEEE, New York, 2009), pp. 17–20.
[48]T. Kubis and P. Vogl, Phys. Rev. B **83**, 195304 (2011).
[49]G. Cahill, W. K. Ford, K. E. Goodson, G. D. Mahan, A. Majumdar, H. J. Maris, R. Merlin, and S. R. Phillpot, J. Appl. Phys. **93**, 793 (2003).